



Structure and magnetic behavior of sol-gel grown spinel $\text{Ni}_x\text{Mn}_{3-x}\text{O}_4$ nanoparticles: Effect of Ni fraction and induction of superparamagnetism at room temperature

Jose Luis Ortiz-Quiñonez^a, Jesús Alberto Ramos Ramón^a, Ma. Eunice de Anda Reyes^a, Apurba Ray^b, Sachindranath Das^b, Umapada Pal^{a,*}

^a Instituto de Física, Benemérita Universidad Autónoma de Puebla, Apdo. Postal J-48, Puebla, 72570, Mexico

^b Department of Instrumentation Science, Jadavpur University, Kolkata, 700032, India

ARTICLE INFO

Keywords:

Nickel manganite
Nanoparticles
Sol-gel synthesis
Magnetic properties
Spinel structure

ABSTRACT

Spinel $\text{Ni}_x\text{Mn}_{3-x}\text{O}_4$ nanostructures have attracted a huge research interest due to their applications in catalysis, electrocatalysis, high-performance supercapacitors, lithium-ion batteries, among others. However, those applications strongly depend on the Ni:Mn ratio, valence states and spatial distribution of cations in the spinel lattice. Using a low-temperature sol-gel process, we synthesized $\text{Ni}_x\text{Mn}_{3-x}\text{O}_4$ nanoparticles of 14–26 nm average sizes with different Ni contents. Effects of Ni incorporation on the morphology, structure and magnetic properties of the nanostructures were studied by SEM, XRD, XPS, Raman spectroscopy and VSM. While a high Ni content in the spinel nanostructures causes lattice shrinkage, lattice expansion at lower Ni content occurs due to higher occupancy of Mn^{2+} ions in tetrahedral sites. Structural and magnetic behaviors of the nanostructures were explained by considering the crystal field stabilization energies of the cations. We demonstrate that superparamagnetic behavior can be induced in the $\text{Ni}_x\text{Mn}_{3-x}\text{O}_4$ nanostructures by incorporating Ni at $x > 1.0$.

1. Introduction

Nickel manganite ($\text{Ni}_x\text{Mn}_{3-x}\text{O}_4$) is a semiconductor with a partially inverse cubic spinel structure, widely used for the fabrication of temperature sensors utilizing its characteristic negative temperature coefficient (NTC) of electrical resistance [1–7]. On the other hand, nanostructures of NiMn_2O_4 have been used as electrocatalysts for urea [8] and water oxidation [9], electrode materials for high-performance supercapacitors [10–12], rechargeable lithium-ion batteries (LIBs) [13], and lithium-air batteries [14]. For these applications, especially for catalytic applications, small-sized nanostructures of ferri(o)magnetic or superparamagnetic nature are desirable. While room temperature superparamagnetism in nickel manganite remains elusive, NiMn_2O_4 nanostructures are frequently obtained as large agglomerates owing to the high temperature (800–900 °C) annealing process used during their fabrication [15–19]. For better performance of these nanostructures in catalysis and energy storage applications, such as in supercapacitors and LIBs, it is necessary to synthesize the $\text{Ni}_x\text{Mn}_{3-x}\text{O}_4$ nanostructures at low temperature to obtain well-dispersed particles with high specific surface

area.

The oxides of manganese can acquire different structural phases such as perovskite, spinel, or pyrochlore depending on the valence state and coordination of Mn ions in their crystal lattice. However, incorporation of Ni can induce structural changes depending on its position in the manganese oxide lattice. Depending on their valence states, the Ni and Mn cations prefer to occupy tetrahedral (T_d) or octahedral (O_h) sites within the cubic close-packed oxygen sub-lattice of the spinel structure. The Mn ions at tetrahedral sites of the Mn_3O_4 lattice have a 2+ valence state, as the Mn^{3+} state is unfavorable in tetrahedral coordination. The incorporation of Ni^{2+} at octahedral sites is compensated by an equal number of Mn^{4+} ions at octahedral sites to retain the charge balance, thus leading to an internal disproportionation [15]. Therefore, the valence state of Mn ions and hence the physical properties of the spinel lattice depend on Ni:Mn ratio. On the other hand, as the effective magnetic moment of a Mn cation depends on its valence state, the Ni content in spinel $\text{Ni}_x\text{Mn}_{3-x}\text{O}_4$ nanoparticles indirectly controls their magnetic properties. Although a few reports on the fabrication of NiMn_2O_4 , $\text{Ni}_{1.5}\text{Mn}_{1.5}\text{O}_4$ and MnNi_2O_4 nanostructures have been

* Corresponding author.

E-mail address: upal@ifuap.buap.mx (U. Pal).

<https://doi.org/10.1016/j.matresbull.2021.111267>

Received 2 August 2020; Received in revised form 24 January 2021; Accepted 10 February 2021

Available online 16 February 2021

0025-5408/© 2021 Elsevier Ltd. All rights reserved.

published in the literature [8,18], effects of Ni:Mn molar ratio on the structure and magnetic properties of the spinel nanostructures have not been studied systematically.

In the present work, we report the synthesis of spinel-like $\text{Ni}_x\text{Mn}_{3-x}\text{O}_4$ nanoparticles with different Ni contents through a glycol-mediated sol-gel process along with their structural and magnetic behaviors. Effects of Ni incorporation on the coordination and valence state of cations in the manganese lattice and their consequence on the magnetic behavior of $\text{Ni}_x\text{Mn}_{3-x}\text{O}_4$ nanoparticles were studied by room-temperature Raman spectroscopy and vibrating sample magnetometry (VSM) in 1.8–300 K temperature range. The effects of Ni content on the size and magnetic behavior of the binary oxide nanoparticles have been discussed considering cation distribution at tetrahedral and octahedral lattice sites.

2. Experimental

For the synthesis of $\text{Ni}_x\text{Mn}_{3-x}\text{O}_4$ nanoparticles with nominal $x = 0.6, 1.0$ and 1.5 , mixtures of $\text{Ni}(\text{CH}_3\text{COO})_2 \cdot 4\text{H}_2\text{O}$ and $\text{Mn}(\text{CH}_3\text{COO})_2 \cdot 4\text{H}_2\text{O}$ in corresponding molar ratios were dissolved in 70 ml of ethylene glycol. The mixtures were magnetically stirred for 10 min, and then 0.15 g of polyvinylpyrrolidone (PVP, FW = 40,000) was added to each of them. The new mixtures were stirred for a further 20 min to obtain transparent solutions. The obtained solutions were heated at 175°C for 4 h putting over a hot oil bath under magnetic agitation and then cooled down to room temperature. The resultant precipitates were separated by centrifugation at 8000 rpm, washed several times with ethanol and distilled water, and dried at 90°C for 48 h. The obtained powders were air-annealed at 300°C for 4 h at a heating rate of $2^\circ\text{C}/\text{min}$ in a muffle furnace. To analyze the morphology and elemental composition of the samples, a small fraction of each of the powder samples was dispersed in ethanol and deposited over Si substrates. A JEOL JSM-7800 F field-emission scanning electron microscope (FESEM) with an attached Oxford X-Max analytic system was utilized to analyze the samples. To estimate the average size of the formed nanoparticles, size distribution

histograms were constructed for each of the samples by estimating the size of individual particles from their FESEM images. To obtain a more accurate particle size distribution, the samples were analyzed in a high-resolution transmission electron microscope (JEOL, JEM 2100 PLUS) operating at 200 kV. A Rigaku MiniFlex600 benchtop diffractometer with a $\text{Cu K}\alpha$ radiation source ($\lambda = 1.542 \text{ \AA}$ generated at 40 kV and 40 mA) was utilized to record the X-ray diffraction (XRD) patterns of the powder samples. Crystallinity and structural phase of the air-annealed samples were further analyzed by Raman spectroscopy at room temperature, utilizing a Horiba Lab RAM HR system equipped with a 633 nm He-Ne laser and a thermoelectrically cooled charge-coupled device (CCD) detector. To estimate the oxidation state of the ions in the samples, X-ray photoelectron spectroscopy (XPS) analysis was carried out in a SPECS GmbH spectrometer (Phoibos 100 MCD Energy Analyzer) using monochromatic $\text{Mg K}\alpha$ radiation (1253.6 eV). The binding energy scale was calibrated by adjusting the position of the C 1s peak arising from adventitious carbon at 284.6 eV. A DynaCool physical properties measurement system (PPMS) of Quantum Design was utilized to measure the magnetic properties of the binary oxides. Magnetization hysteresis ($M-H$) loops of the samples were recorded at different temperatures (1.8, 40, 100, and 300 K) under magnetic fields up to 7.0 T. Temperature-dependent magnetizations were recorded under constant magnetic fields of 50 and 500 Oe in 1.8–300 K temperature range.

3. Results and discussion

Fig. 1 presents typical SEM images of the synthesized $\text{Ni}_x\text{Mn}_{3-x}\text{O}_4$ samples with different Ni contents. As can be seen, all the samples contain agglomerated spherical particles of nanometric dimensions. Observed agglomeration of particles in the samples is probably due to the magnetic interaction among the small particles with high surface energy. The average size of the particles in the mixed oxide decreased with the increase of Ni content (Table 1), probably due to the formation of additional phases that restricted their growth during synthesis. The representative EDS spectrum of the NiMn_2O_4 nanoparticles (Ni:Mn =

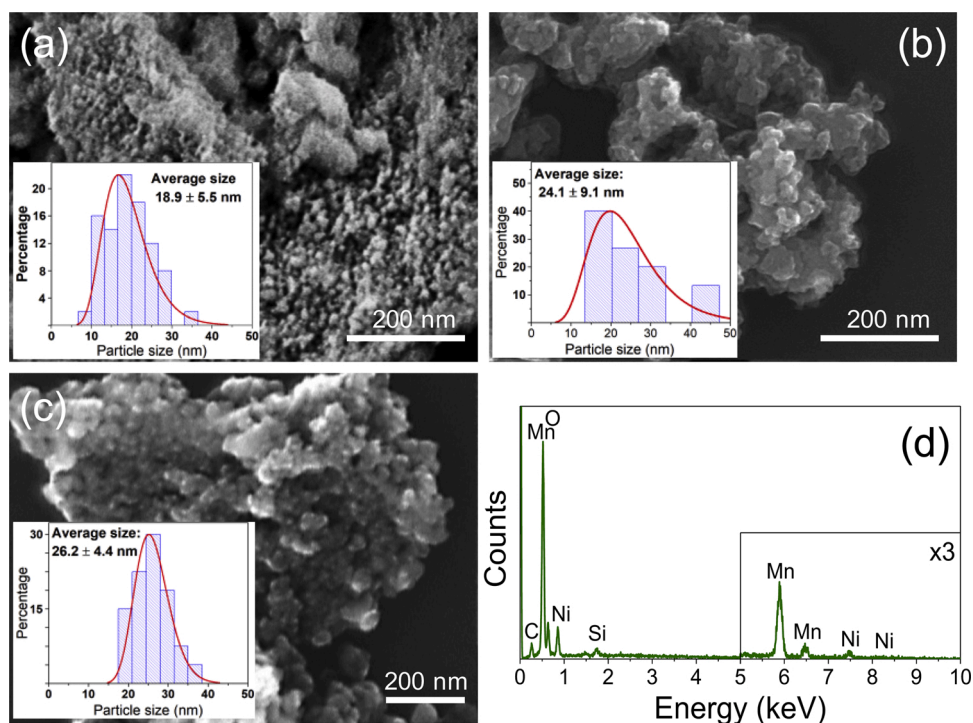


Fig. 1. Typical SEM images of the Ni-Mn oxide nanoparticles synthesized using (a) 1:1, (b) 1:2, and (c) 1:4 M ratios of Ni and Mn precursors. (d) Representative EDS spectrum of the NiMn_2O_4 nanoparticles (Ni:Mn = 1:2). The 5–10 keV range of the EDS spectrum has been zoomed-in for a better display of the high-energy ($\text{K}\alpha$) Mn and Ni signals.

Table 1

Elemental composition and estimated average particle size of the $\text{Ni}_x\text{Mn}_{3-x}\text{O}_4$ samples with different Ni contents.

Nominal Ni:Mn ratio	Ni (at %)		Mn (at %)		O (at %)		Av. Particle size (nm)	
	EDS	XPS	EDS	XPS	EDS	XPS	SEM TEM	
							SEM	TEM
1:1	27.1	25.1	19.4	22.3	53.5	52.6	18.9	—
1:2	11.8	14.4	27.7	30.7	60.5	54.9	24.1	14.9
1:4	10.0	11.1	29.6	38.8	60.4	50.1	26.2	16.6

Standard deviation for the compositions estimated through EDS was ± 0.5 at %.

1:2) presented in Fig. 1d clearly indicates the absence of foreign elements, confirming the high purity of the fabricated nanostructures. Elemental compositions of the samples obtained by averaging the composition estimated at five different positions of each of the samples are presented in Table 1. While a small oxygen excess could be detected in the samples prepared with nominal $x = 0.6$ and 1.0 , for $x = 1.5$, the sample became oxygen deficient. Such an oxygen deficiency in the sample containing the highest Ni content is probably due to the presence of nickel nanoparticles. As reported by Larcher and Patrice, boiling ethylene glycol can reduce Ni^{2+} ions and NiO nanoparticles to metallic nickel nanoparticles [20]. Moreover, the estimated Ni content in the latter sample is much higher than its nominal value, contrary to the other two samples where the estimated Ni contents are slightly lower than their nominal values.

Fig. 2 presents the TEM images of the Ni-Mn oxide nanoparticles synthesized at 1:2 and 1:4 M ratios of nickel and manganese. Average particle sizes in the samples estimated from their TEM micrographs were 14.9 ± 4.0 and 16.6 ± 3.4 nm, respectively. As can be noticed, the TEM estimated average particle sizes of the samples are slightly smaller than the sizes estimated from their SEM images. This discrepancy can be attributed to the high agglomeration of the particles in the samples prepared for SEM analysis. The better dispersion of particles in the TEM samples can be easily noticed from the micrographs presented in Fig. 2.

Fig. 3 presents the XRD patterns of the $\text{Ni}_x\text{Mn}_{3-x}\text{O}_4$ samples recorded in the $20 - 80^\circ$ range. The NiMn_2O_4 nanoparticles (Ni:Mn = 1:2) revealed their spinel-like crystal structure (JCPDS card #01-1110) [14]. As can be noticed in the XRD patterns (Fig. 3), the samples prepared with Ni:Mn molar ratios of 1:1 and 1:2 revealed diffraction peaks at higher angles compared to their positions in the sample prepared with Ni:Mn =

1:4, indicating lattice shrinkage due to Ni incorporation (Table 2). On the other hand, the relative intensities of the main diffraction peaks such as (311), (400) and (440) in the sample with Ni:Mn = 1:1 are very different from their relative intensities in the other two samples (i.e., Ni:Mn = 1:2 and 1:4). For example, in contrast to the former sample (Ni:Mn = 1:1), intensity of the (311) peak in the latter two samples is much higher than the intensities of the (400) and (440) peaks. The higher intensity of the (400) and (440) peaks in the samples with Ni:Mn = 1:1 is probably due to their overlapping with the (200) and (220) peaks of NiO (JCPDS card # 78-0429). Moreover, there appeared two additional diffraction peaks around $2\theta = 44.5$ and 51.8° in this (Ni:Mn = 1:1) sample, which correspond to metallic nickel (Ni^0) in cubic phase (JCPDS card # 004-0850). Formation of metallic Ni in the sample indicates a reduction of Ni ions by ethylene glycol during the synthesis process. Presence of additional phases (NiO and Ni nanoparticles) restrained the growth of $\text{Ni}_x\text{Mn}_{3-x}\text{O}_4$ nanoparticles [21]. In fact, a reduction of particle size and an oxygen-deficient composition for the Ni:Mn = 1:1 sample (Table 1) were observed in its SEM-EDS analysis. Such a formation of NiMn_2O_4 and NiO nanoparticle mixture has also been observed earlier in air-annealed (800°C , 3 h) nickel manganites with a Ni:Mn molar ratio of 1:1 [8,18].

Using Rietveld refinement of neutron powder diffraction data, Ferreira et al. obtained the cation distribution $\text{Ni}_{0.2}\text{Mn}_{0.8}[\text{Ni}_{0.84}\text{Mn}_{1.16}]\text{O}_4$ for their NiMn_2O_4 sample [22]. Similarly, Díez et al. obtained a cation distribution $\text{Ni}^{2+}_{0.0965}\text{Mn}^{2+}_{0.865}[\text{Ni}^{2+}_{0.865}\text{Mn}^{3+}_{0.265}\text{Mn}^{4+}_{0.865}]\text{O}_4$ for the same oxide by Rietveld refinement of X-ray diffraction data [15]. On the other hand, Åsbrink et al. reported a cation distribution $\text{Ni}^{2+}_{0.2}\text{Mn}^{2+}_{0.8}[\text{Ni}^{2+}_{0.8}\text{Mn}^{3+}_{0.4}\text{Mn}^{4+}_{0.8}]\text{O}_4$ for a NiMn_2O_4 single crystal by refining its X-ray diffraction data [23]. In these distributions, the cations outside and inside the brackets correspond to the ions at tetrahedral (T_d) and octahedral (O_h) lattice sites, respectively. In all these distributions, the Mn^{2+} ions remain at T_d sites, Mn^{3+} and Mn^{4+} ions remain at O_h sites, while Ni^{2+} ions prefer to be located at O_h sites. To explain these observations, a schematic of crystal field splitting (Δ) and crystal field stabilization energies (CFSE) for these cations are shown in Fig. 4. The Δ and CFSE values for the Ni or Mn cations at O_h and T_d sites in oxides have been reported in ref. [24]. The reported CFSE values for Ni^{2+} , Mn^{2+} and Mn^{3+} cations at T_d (O_h) sites are -39.7 (-125.8), 0 (0) and -44.6 (-142.2) kJ mol^{-1} , respectively. Although the CFSE value for the Mn^{4+} ion has not been reported in the literature, it can be assumed to be similar to that of Cr^{3+} ion as both the ions have same outer shell electronic

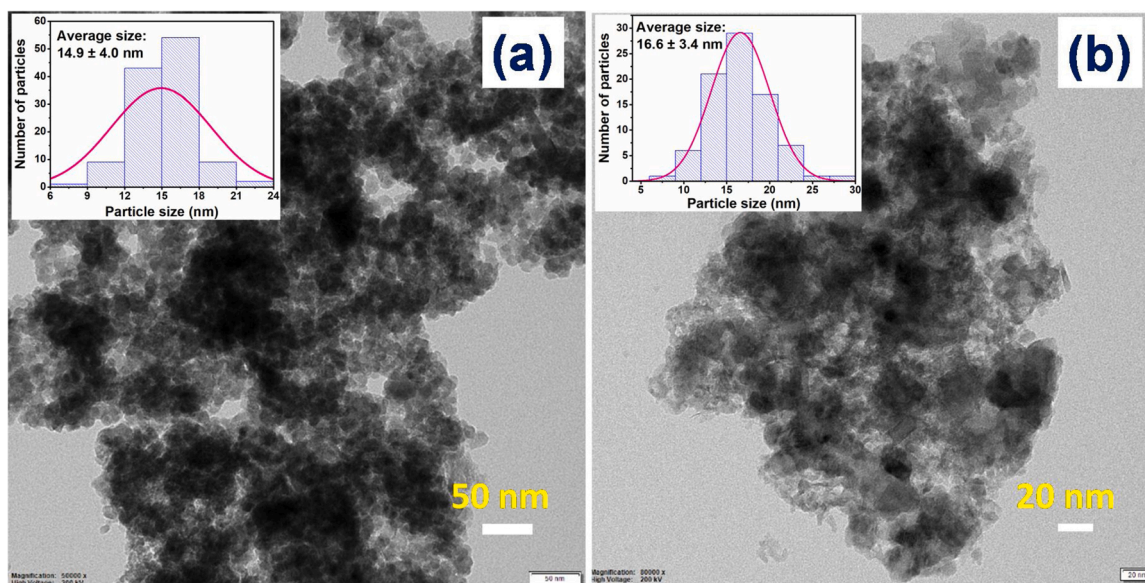


Fig. 2. Typical TEM images of the Ni-Mn oxide nanoparticles synthesized with (a) 1:2 and (b) 1:4 M ratios of Ni and Mn precursors. Insets in (a) and (b) are the size distribution histograms of corresponding samples.

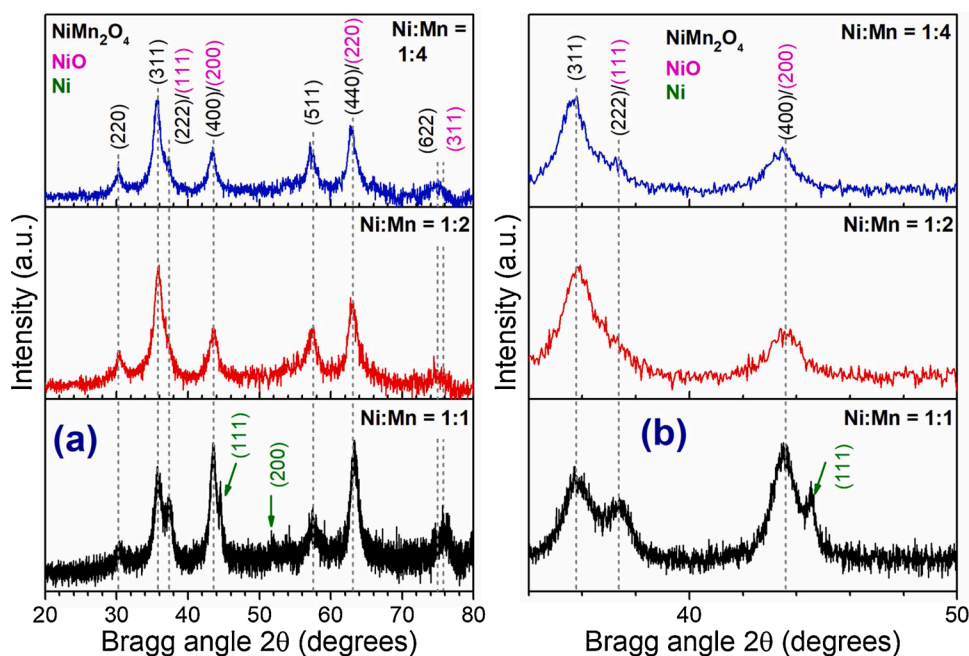


Fig. 3. Room temperature XRD patterns of the Ni-Mn oxide samples prepared with different Ni:Mn molar ratios. The diffraction peaks indicated by green and magenta colors correspond to the diffraction from metallic Ni (JCPDS card # 04-0850) and NiO (JCPDS card # 78-0429), respectively. (b) Amplification of figure (a) in the range $2\theta = 34 - 50^\circ$.

Table 2

XRD peak positions and estimated lattice parameters for the $Ni_xMn_{3-x}O_4$ nanostructures with different Ni contents.

Ni:Mn ratio	(hkl)	Bragg angle ($^\circ$)	Lattice parameter (Å)
1:1	(311)	35.82	8.30
	(400)	43.57	8.30
1:2	(311)	35.81	8.31
	(400)	43.54	8.31
1:4	(311)	35.63	8.34
	(400)	43.35	8.34

configuration, i.e. $[Ar]3d^3$.

Keeping in mind the above observations and CFSE values, a tentative cation distribution for our nickel manganite sample with a Ni:Mn ratio of 1:4 can be expressed as $Ni^{2+}_{0.1}Mn^{2+}_{0.9}[Ni^{2+}_{0.5}Mn^{3+}Mn^{4+}_{0.5}]O_4$.

However, a cation distribution such as $Ni^{2+}_{0.2}Mn^{2+}_{0.1}Mn^{3+}_{0.6}[Ni^{2+}_{1.2}Mn^{4+}_{0.8}]O_4$ or $Ni^{2+}[Ni^{2+}_{0.5}Mn^{3+}Mn^{4+}_{0.5}]O_4$ is improbable for the sample prepared with a Ni:Mn ratio of 1:1, as a high content of Mn^{3+} or Ni^{2+} ions at T_d sites makes the nickel manganite unstable. A probable cation distribution for this sample could be $Ni^{2+}_{0.2}Mn^{2+}_{0.8}[Ni^{2+}Mn^{4+}]O_4$, where all the Mn^{3+} ions at O_h sites are oxidized to Mn^{4+} to fulfill the charge electroneutrality condition in the spinel lattice. The remaining nickel ions form Ni and NiO byproducts. The analysis presented above explains why NiO and Ni phases were formed in the sample prepared with Ni:Mn of 1:1 sample, but not in the other two samples. It is worth mentioning that an increase of Ni^{2+} ions at O_h sites also increases the percentage of Mn^{4+} ions at O_h sites (by oxidation of Mn^{3+} ions) to maintain the charge electroneutrality of the lattice. Since the Mn^{4+} ion is considerably smaller (0.53 Å) than the Mn^{3+} ion (0.645 Å), increasing the percentage of Ni^{2+} ions in the lattice generates a small shrinkage of

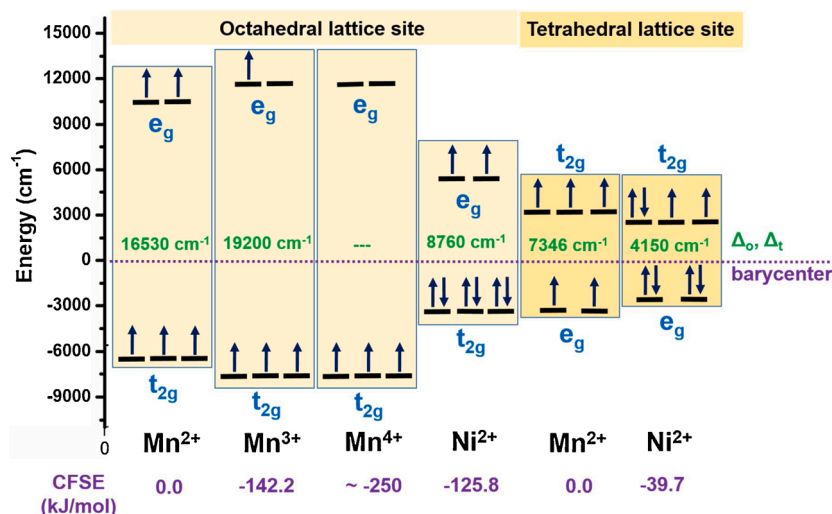
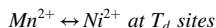
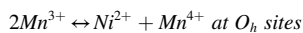


Fig. 4. Schematic representation of crystal field splitting for the cations present in $Ni_xMn_{3-x}O_4$ lattice along with their crystal field stabilization energies (CFSE) at O_h and T_d sites (bottom). The values were taken from Refs. [24,26].

the unit cell (Fig. 3 and Table 2).

Taking the cation distribution $\text{Ni}^{2+}_{0.2} \text{Mn}^{2+}_{0.8}[\text{Ni}^{2+}_{0.8} \text{Mn}^{3+}_{0.4} \text{Mn}^{4+}_{0.8}]\text{O}_4$ proposed by Åsbrink et al. for NiMn_2O_4 [23] as a starting point, the situations that must occur in the lattice when additional Ni^{2+} ions are incorporated at O_h and T_d sites to maintain the charge electroneutrality can be presented by the relations:



Note that once all the Mn^{3+} ions at O_h sites are oxidized to Mn^{4+} , no more Ni^{2+} ions can be incorporated into the lattice. The excess nickel ions incorporated in the reaction mixture form NiO and Ni^0 as byproducts, as has been observed in the sample prepared with a nominal Ni:Mn ratio of 1:1. Substitution of Mn^{2+} by Ni^{2+} ions at T_d sites is energetically less favorable than forming NiO . Hence, there is a maximum limit for Ni^{2+} ion content in the $\text{Ni}_x\text{Mn}_{3-x}\text{O}_4$ spinel lattice. Moreover, the reported ionic radii for Mn^{2+} , Ni^{2+} and Mn^{3+} ions at O_h sites are 0.83, 0.69 and 0.645 Å, respectively, which means that Mn^{2+} is 0.14 Å larger than Ni^{2+} ion, and 0.185 Å larger than that of Mn^{3+} ion [25]. A similar difference in ionic radii is expected between the Mn^{2+} and Ni^{2+} ions at T_d sites. A decrease in Ni:Mn ratio in the sample increases the $\text{Mn}^{2+}/\text{Ni}^{2+}$ ratio at T_d sites. As a result, the crystal lattice tends to expand, and the XRD peaks shift to lower Bragg angles.

To study the variation of the valence state of Mn cations in $\text{Ni}_x\text{Mn}_{3-x}\text{O}_4$ samples with different Ni:Mn molar ratios, we performed their XPS

analysis, recording survey spectra and core-level spectra of Mn 2p_{3/2}, Ni 2p_{3/2} and O 1s orbitals (Fig. 5). As expected, Mn, Ni, O and C could be detected in the survey spectra of the samples (Fig. 5a). Traces of Na were also detected in the samples (binding energy, BE =899 eV), which probably came from the glassware used for sample handling or ceramic crucible used for sample annealing. Presence of Ni in the samples was confirmed by the appearance of the L₂M₂₃M₄₅ Auger line (around 408 eV) in their survey spectra (Fig. 5b). Intensity of the Auger line increased for higher Ni:Mn ratios (nominal). Although the signal-to-noise ratios in the core level spectra of nickel were very low for all the samples, a small emission band could be detected around 853.5 eV (Fig. 5c) for the sample with Ni:Mn of 1:1, which corresponds to the Ni 2p_{3/2} emission. The core-level emission bands of oxygen and manganese (O 1s and Mn 2p_{3/2}) were deconvoluted to extract the positions and relative areas of the component bands (Table 3). The O 1s orbital emission band could be deconvoluted into three components (Fig. 5d-f). While the component 1, centered at ~ 529 eV, corresponds to the oxygen bonded to Mn²⁺ ions, the component 2 is associated to the oxygen bonded to both the Mn^{3+/4+} and Ni²⁺ ions (either in the Ni_xMn_{3-x}O₄ phase or in the NiO impurity). On the other hand, the component 3 centered in between 531.3 and 532.2 eV is associated to the M—OH (M = Ni, Mn) species present at the surface of the Ni_xMn_{3-x}O₄ nanoparticles (Table 3) [27]. As can be noticed in Table 3, the relative area and intensity of the component 2 are higher for the sample with a Ni:Mn ratio of 1:1, compared with those of the other two samples (Ni:Mn = 1:2 and 1:4 ratio). The difference might be due to the presence of a larger quantity of Ni-O bonds in the former

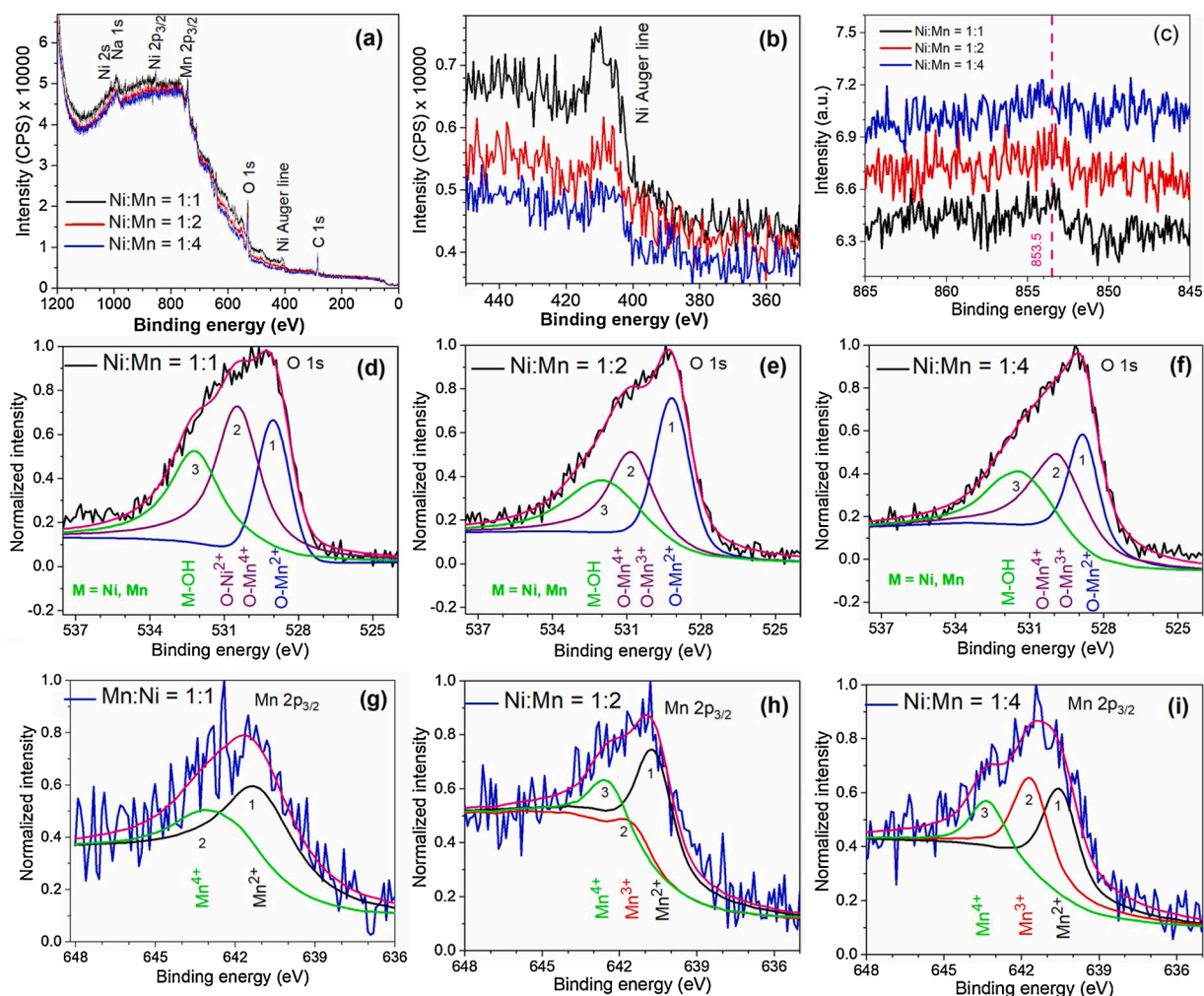


Fig. 5. (a) XPS survey spectra, (b) amplified survey spectra near the Auger line of nickel, and high-resolution XPS spectra of (c) Ni 2p_{3/2}, (d-f) O 1s and (g-i) Mn 2p_{3/2} for the $\text{Ni}_x\text{Mn}_{3-x}\text{O}_4$ samples with nominal Ni:Mn ratios of 1:1, 1:2 and 1:4.

Table 3

Binding energy (BE, eV) and area (%) of the components of representative XPS emissions for the $\text{Ni}_x\text{Mn}_{3-x}\text{O}_4$ samples with three nominal Ni:Mn ratios.

Sample (nominal Ni: Mn)	Emission (orbital)	Binding energy (eV) and areas (A, %)			Ratio of peak area
		fit peak 1 (A1)	fit peak 2 (A2)	fit peak 3 (A3)	
Ni:Mn = 1:1	O 1s	529.00 (23.2 %)	530.45 (44.0 %)	532.17 (32.8 %)	(A1)/ (A2) = 0.53
Ni:Mn = 1:2	O 1s	529.16 (37.2 %)	530.8 (32.5 %)	531.89 (30.3 %)	(A1)/ (A2) = 1.14
Ni:Mn = 1:4	O 1s	528.82 (32.3 %)	529.85 (38.4 %)	531.35 (29.3 %)	(A1)/ (A2) = 0.84
Ni:Mn = 1:1	Mn 2p _{3/2}	641.14 (60.72 %)	642.55 (39.28 %)	—	(A1)/ (A2) = 1.54
Ni:Mn = 1:2	Mn 2p _{3/2}	640.65 (59.90 %)	641.46 (14.73 %)	642.43 (25.37 %)	(A1)/ (A3) = 2.36
Ni:Mn = 1:4	Mn 2p _{3/2}	640.51 (41.23 %)	641.63 (37.74 %)	643.28 (21.02 %)	(A1)/ (A3) = 1.96

sample.

Deconvolution of the Mn 2p_{3/2} peaks and corresponding valence states of Mn ions in the samples are presented in Fig. 5g-i. According to the values reported in the literature, the BE of Mn²⁺, Mn³⁺, and Mn⁴⁺ ions in corresponding oxides appear at ~640.3 eV, ~641.2 eV, and ~642.0 eV, respectively [27–29]. Following the same, we found three valence states of the Mn ions for the sample with a Ni:Mn ratio of 1:2 (Fig. 5h), in good agreement with the cation distribution Ni²⁺_{0.0965}Mn²⁺_{0.865}[Ni²⁺_{0.865}Mn³⁺_{0.265}Mn⁴⁺_{0.865}]O₄ proposed earlier (in the XRD section). The lower relative area of the component peak associated with Mn³⁺ ion in the spectrum is in accordance with the lower mole fraction (0.265) of the Mn³⁺ cation in the sample (Ni:Mn = 1:2). Likewise, three valence states for the Mn ion could be detected in the sample with a Ni:Mn ratio of 1:4 (Fig. 5i), which is in accordance with the proposed cation distribution Ni²⁺_{0.1}Mn²⁺_{0.9}[Ni²⁺_{0.5}Mn³⁺_{0.5}]O₄ suggested in the XRD section. It should be noted (Fig. 5i) that the component with the smallest relative area in this sample corresponds to the Mn⁴⁺ ion, which further supports the cation distribution we suggested. Finally, two valence states for the Mn ion could be detected for the sample with the nominal Ni:Mn ratio of 1:1 (Fig. 5g), which is in accordance with the cation distribution Ni²⁺_{0.2}Mn²⁺_{0.8}[Ni²⁺_{0.2}Mn⁴⁺_{0.8}]O₄ we suggested for the sample. It is worth mentioning that the knowledge of valence states of Mn ions in inverse-spinel nanostructures is extremely valuable to explain their magnetic behaviors. In the following section, we analyze the magnetic behavior of the nanostructures considering their cation distribution at tetrahedral and octahedral sites.

Room-temperature Raman spectra of the fabricated nanostructures were recorded in the 300–900 cm⁻¹ spectral range. As can be seen in Fig. 6, there appeared an intense Raman band at 643 cm⁻¹ and three low-intensity dispersion bands around 429, 507, and 708 cm⁻¹ for the Ni:Mn = 1:4 and 1:2 samples. The positions of these dispersion bands are very close to the reported positions of the common vibrational modes of the NiMn₂O₄ spinel structure [16,30,31]. On the other hand, six vibrational modes were revealed around 429, 452, 492, 576, 643 and 708 cm⁻¹ for the sample with Ni:Mn of 1:1. The bands appeared around 576 and 643 cm⁻¹ are attributed to the stretching vibrations of the Mn-O bond at O_h sites, in which the oxidation states of Mn ions are +2 and +3, respectively [32,33]. Considering that the highest bond strength in

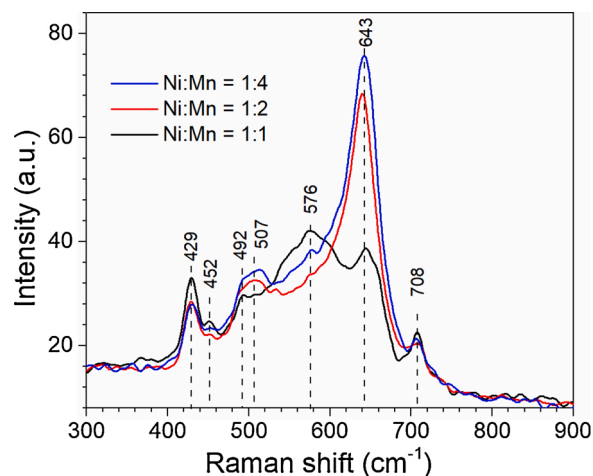


Fig. 6. Raman spectra of the Ni-Mn oxide samples prepared with different Ni:Mn molar ratios.

nickel manganites corresponds to the Mn⁴⁺-O bond, the band revealed at the highest energy position (708 cm⁻¹) could be assigned to the Mn⁴⁺-O stretching mode in the MnO₆ octahedra [34]. The band revealed around 429 cm⁻¹ is associated with a bending mode, position of which depends on the distribution of cations at O_h and T_d sites [32]. While the broad band appeared near 576 cm⁻¹ corresponds to NiO [35], the dispersion band appeared around 452 cm⁻¹ has been previously associated with the activation of Raman vibration induced by magnetostriction effect at low temperatures. Magnetostriction effect has been considered to be responsible for a slight rhombohedral distortion of bulk NiO [36].

As can be seen in Fig. 6, the intensity of the 643 cm⁻¹ band reduced significantly in the highest Ni content (Ni:Mn = 1:1) sample. Such intensity reduction and broadening of vibrational mode of the spinel-like crystal lattice are caused by lattice distortion on Ni incorporation [37, 38]. In agreement with the XRD results, on increasing the Ni content in the mixed oxide nanostructures, relative intensity of the band associated with the Ni-O vibrational mode increased. The result indicates the formation of a secondary nickel oxide phase due to nickel segregation in the Ni:Mn = 1:1 sample, or the formation of ethylene glycol–nickel complexes at the surface of the nanoparticles. The nickel–ethylene glycol complexes formed during synthesis are fairly stable, which probably were not completely decomposed or removed during air annealing of the nanostructures at the low annealing temperature (300 °C) used in the present study [39]. Appearance of a significant carbon (C) signal in the EDS spectra of the annealed nanostructures (Fig. 1d) also confirms this fact.

Fig. 7 shows the zero-field cooling and field cooling (ZFC-FC) curves of the Ni_xMn_{3-x}O₄ nanoparticles recorded under two different applied magnetic fields (50 and 500 Oe). To avoid artifacts due to the trapped field in the superconducting magnet of PPMS, measurements were carried out with the application of sequential positive and negative (oscillating) fields. As can be seen, the sample prepared with a Ni:Mn ratio of 1:1 has the highest magnetization, irrespective of applied magnetic field or measured temperature. While the revealed blocking temperature (T_B) of the stoichiometric (Ni:Mn = 1:2) sample (55 K) is within the range of its reported values (50–60 K) [18], the T_B is a bit higher (61 K) for the sample with the lowest Ni content (i.e. Ni:Mn = 1:4). T_B represents the temperature at which the thermal energy ($k_B T$) is comparable to the energy barrier (ΔE) that must be overcome before a particle can reverse its magnetization ($\Delta E = K_u V$), where k_B , T , K_u and V represent the Boltzmann constant, absolute temperature, anisotropy energy density, and volume of the nanoparticle, respectively [40,41]. Such an abnormal behavior is also noticed in the FC curve of the sample prepared with Ni:Mn of 1:2, which revealed a change of slope around 55

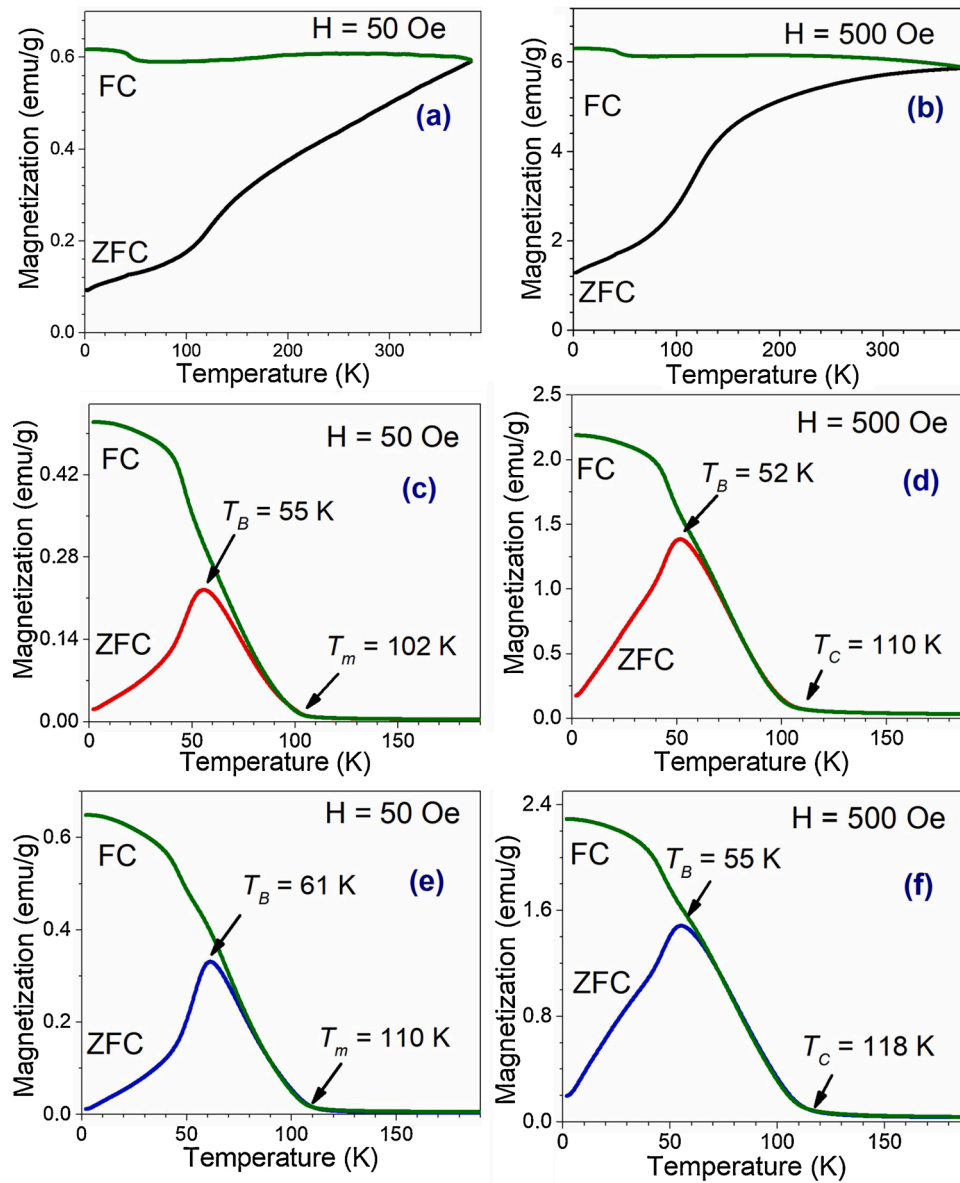


Fig. 7. Magnetization versus temperature plots for the $\text{Ni}_x\text{Mn}_{3-x}\text{O}_4$ samples with Ni:Mn ratios of (a,b) 1:1, (c,d) 1:2, and (e,f) 1:4. The closed triangles denote the FC curves and the open triangles correspond to the ZFC curves.

and 52 K for the 50 and 500 Oe applied fields, respectively. The Curie temperature (T_C), which is the temperature where the ferrimagnetic-paramagnetic transition occurs, remained in-between 100 and 120 K for the Ni:Mn = 1:2 and 1:4 samples (Fig. 7c-f). The results are in well accordance with the reported T_C values for NiMn_2O_4 nanoparticles of 10–15 nm sizes (126 K), nanorods of 150 nm \times 350 nm dimensions (118 K) and NiMn_2O_4 single crystal (130–145 K) [23,42].

Upon increasing the applied magnetic field from 50 Oe to 500 Oe, both T_B and T_C of the samples with Ni:Mn = 1:2 and 1:4 decreased, as expected, due to the reduction of energy barriers by the external field, allowing reorientation of the magnetic domains by thermal fluctuations at lower temperatures [43]. A higher applied field provides more energy to the magnetic domains, increasing their magnetization and reducing the T_B . However, a different behavior is observed in the (M - H) plot of the Ni:Mn = 1:1 sample, where the T_C is above room temperature. The sample revealed no well-defined blocking temperature, as it manifested a superparamagnetic behavior over the entire measurement temperature range (1.8–300 K). Such a distinct behavior of the $\text{Ni}_x\text{Mn}_{3-x}\text{O}_4$ nanostructures prepared with a nominal Ni:Mn ratio of 1:1 is probably

associated with higher super-exchange coupling due to the high Mn^{4+} and Ni^{2+} ion contents at O_h sites.

The magnetization (M) vs. magnetic field (H) curves of the samples recorded at different temperatures are displayed in Fig. 8. It can be seen that the magnetization of the $\text{Ni}_x\text{Mn}_{3-x}\text{O}_4$ nanoparticles has both ferromagnetic/superparamagnetic and paramagnetic components (Fig. 8, left column). The sample prepared with a Ni:Mn ratio of 1:1 shows superparamagnetic behavior, even at 300 K, with enhanced saturation magnetization (M_s), compared to the other two samples (Fig. 8). For all the samples, magnetization did not saturate; rather varied linearly at higher magnetic fields, indicating a small paramagnetic contribution, probably due to uncompensated spins at the surface of the nanoparticles. To eliminate the paramagnetic contribution from the magnetization data of the nanostructures, we subtracted the diamagnetic contribution ($\chi_d = 9.11 \times 10^{-5}$, 8.12×10^{-5} and 7.62×10^{-5} $\text{emu g}^{-1} \text{Oe}^{-1}$ for $T = 1.8$, 40, and 100 K, respectively) [44] from the magnetization curves, as shown in Fig. 8b, d, and f. As can be seen, after the subtraction of paramagnetic components, the (M - H) curve of the Ni:Mn = 1:1 sample exhibits a superparamagnetic behavior with $M_s \approx 13.1$ emu/g . On the

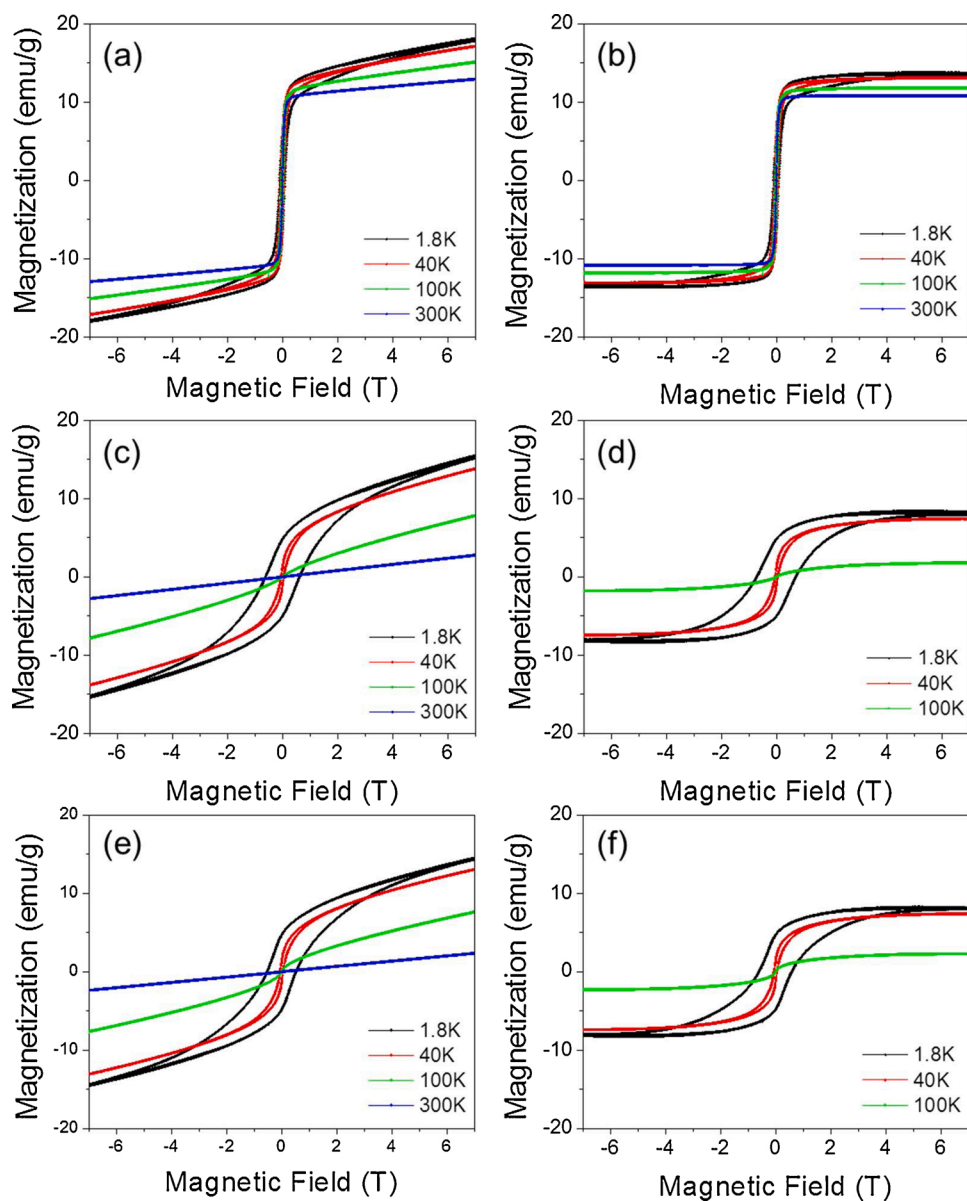


Fig. 8. Magnetization hysteresis curves recorded at different temperatures for the $\text{Ni}_x\text{Mn}_{3-x}\text{O}_4$ samples (left column) and their respective paramagnetic-component corrected curves (right column) for $x =$ (a,b) 1.5, (c,d) 1.0, and (e,f) 0.6.

other hand, after the subtraction of paramagnetic component, the other two samples (Ni:Mn = 1:2 and 1:4) revealed ferrimagnetic behavior ($M_s \approx 8.4$ and 8.2 emu/g for the samples with Ni:Mn ratios of 1:2 and 1:4, respectively) up to 40 K. However, the ferrimagnetic behavior of the samples changed to paramagnetic at higher temperatures.

Air-annealed (800–900 °C) micro- and sub-micrometric NiMn_2O_4 particles (0.2–2 μm) showed their superparamagnetic behavior at low temperatures (< 25 K) with reported M_s values between 15 and 37.5 emu/g [15,18,19,45–49]. However, at room temperature, they exhibit paramagnetic behavior [45,47]. In contrast, the nanoparticles in the sample with Ni:Mn ratio of 1:1 revealed superparamagnetic behavior in the 1.8–300 K temperature range. Although traces of Ni nanoparticles were detected in the XRD pattern of this sample, the amount of nickel might not be enough to account for the M_s value (13.1 emu/g) it revealed at 1.8 K. For the sake of comparison, the reported room-temperature M_s value for nickel nanoparticles of 16 nm size is ~ 27 emu/g [50]. Furthermore, the NiO detected in this sample does not contribute to the M_s value because of its antiferromagnetic nature ($T_{\text{Néel}} \sim 525$ K) [49,51].

For the nanoparticles with lower Ni mole fractions such as $x = 0.6$ and 1.0, the observed ferrimagnetism is caused by the contribution of cation sub-lattices (Ni^{2+} , Mn^{2+} , Mn^{3+} and Mn^{4+}) of the spinel [22]. Being monometallic oxides, while Mn_3O_4 nanoparticles (with a combination of Mn valence states 2+ and 3+) show a ferrimagnetic behavior below 42 K [52,53], NiO (with Ni valence state 2+) nanostructures show antiferromagnetic behavior below 523 K [54]. The combination of these two oxides in the spinel $\text{Ni}_x\text{Mn}_{3-x}\text{O}_4$ nanoparticles gives rise to a ferrimagnetic behavior due to exchange coupling among the cation sub-lattices [22]. Moreover, each Ni^{2+} cation introduced in the O_h lattice sites causes the oxidation of one Mn^{3+} ion to form Mn^{4+} ion. The typical values of effective magnetic moments for the Ni^{2+} , Mn^{2+} , Mn^{3+} and Mn^{4+} ions are 3.25, 5.85, 4.85 and 3.8 μ_B , respectively [55]. Hence, the oxidation of Mn^{3+} to Mn^{4+} induced by the incorporated Ni^{2+} cation affects the magnetic properties of the binary oxide. The results clearly demonstrate that magnetic behaviors of the $\text{Ni}_x\text{Mn}_{3-x}\text{O}_4$ nanoparticles can be controlled by tuning the Ni fraction in $\text{Ni}_x\text{Mn}_{3-x}\text{O}_4$ nanoparticles.

From the temperature evolutions of the saturation magnetization (M_s) and coercive field (H_c) of the $\text{Ni}_x\text{Mn}_{3-x}\text{O}_4$ nanoparticles presented in

Fig. 9, we can see that the variations of M_s and H_c are very similar for the Ni:Mn = 1:4 and 1:2 samples for the entire temperature range. Notably, the H_c values obtained for these samples are significantly higher than the literature reported values for NiM₂O₄ [19,46–49,56]. On the other hand, for the Ni:Mn: 1:1 sample, both the M_s and H_c decreased gradually with temperature. At lower temperatures, the H_c value of the sample (Ni:Mn = 1:1) is quite low, while its M_s is quite high in comparison to that of the other two samples. The distinctive variations of M_s and H_c observed for the sample (Ni:Mn: 1:1) with respect to the other two samples (Ni:Mn = 1:4 and 1:2) are associated with its superparamagnetic nature (Fig. 8). The cation sub-lattices (A and B) contribute to the magnetic properties in different ways, depending on their chemical environments [57]. In insulator oxides such as Ni_xMn_{3-x}O₄, the magnetic interaction between the cations is derived from superexchange interactions [58]. This magnetic interaction dictates the spin alignment and hence the M_s value. In materials with spinel structure, the cations at T_d sites (sub-lattice A) are aligned parallel among themselves. Likewise, the cations at O_h sites (sub-lattice B) are aligned parallel among themselves, but antiparallel to the cations at T_d sites. However, in the case of NiMn₂O₄, the cations are not completely antiparallel, i.e. non-collinear, as shown schematically in Fig. 10 [22,47]. The non-collinear character of cationic spins has been reported by Goodenough in spinels, in which the T_d sites are occupied by Mn²⁺ ions and O_h sites are occupied by the ions with half-filled t_{2g} orbitals (e.g., Mn⁴⁺ in the present work) [59]. Therefore, the M_s values of the Ni_xMn_{3-x}O₄ nanoparticles (for $x > 0$) are not simply the differences between the net magnetic moments contributed by the ions in the sub-lattices A and B. However, Díez et al. calculated the M_s values for Ni_{0.96}Mn₂O₄ particles by adding all contributions on the octahedral sites (Ni²⁺ = 2 μ_B ; Mn²⁺ = 5 μ_B ; Mn³⁺ = 4 μ_B ; Mn⁴⁺ = 3 μ_B) and subtracting the corresponding contributions on the tetrahedral sites [15]. In Table 4, we present the reported M_s values for Ni_xMn_{3-x}O₄ particles along with the values obtained in the present work. As can be noticed (Table 4), the reported M_s values for submicrometric NiMn₂O₄ particles are in-between 15 and 45 emu/g. However, the experimentally obtained M_s values for the smaller NiMn₂O₄ (i.e., Ni:Mn = 1:2) particles are considerably lower. Such differences might be due to the lower crystallinity of the nanoparticles.

Using the procedure used by Díez et al., the M_s values for our Ni_xMn_{3-x}O₄ nanostructures with Ni:Mn molar ratios of 1:1, 1:2, and 1:4 were calculated using the cation distributions Ni²⁺_{0.2}Mn²⁺_{0.8}[Ni²⁺Mn⁴⁺]_{0.8}O₄, Ni²⁺_{0.2}Mn²⁺_{0.8}[Ni²⁺_{0.8}Mn³⁺_{0.4}Mn⁴⁺_{0.8}]_{0.8}O₄, and Ni²⁺_{0.1}Mn²⁺_{0.9}[Ni²⁺_{0.5}Mn³⁺Mn⁴⁺_{0.5}]_{0.5}O₄, respectively. As can be noticed (Table 4), the experimentally obtained M_s value for the sample with a Ni:Mn molar ratio of 1:1 is close to its calculated value. Nonetheless, metallic nickel present in the sample (as impurity) contributed to the measured M_s value. In the case of the samples with Ni:Mn molar ratios of 1:2 and 1:4, the experimental M_s values were considerably lower than the calculated values. The differences can be attributed to (i) the low crystallinity of the samples, (ii) non-consideration of spin-orbit coupling

in the materials containing Ni²⁺, Mn³⁺ and Mn⁴⁺ ions in the calculation of M_s values, and (iii) overestimation of M_s value due to considering simply the differences between the net magnetic moments contributed by the ions in the sub-lattices A and B, as discussed earlier.

Finally, it should be mentioned that the Curie temperature is also sensitive to the structure of the nickel manganite lattice, Ni:Mn ratio, and valence state of the cations. A good example of this dependence is the high T_c value (430 K) observed for NiMnO₃ particles in ilmenite phase, which have only Ni²⁺ and Mn⁴⁺ ions, all at O_h sites [60]. The high T_c value manifested by the spinel particles fabricated in the present work with a nominal Ni:Mn ratio of 1:1 is probably due to the presence of only Ni²⁺ and Mn⁴⁺ ions at O_h sites.

4. Conclusions

In summary, using a simple glycol-mediated process, we fabricated Ni_xMn_{3-x}O₄ nanoparticles of different Ni contents in the 14–26 nm average size range. While a lower Ni fraction produces larger nanoparticles, incorporation of Ni in a higher mole fraction causes the formation of NiO and Ni byproducts at the surface of the formed nanoparticles, restricting their further growth. The spinel Ni_xMn_{3-x}O₄ nanoparticles with Ni:Mn ratios of 1:4 and 1:2 manifest their ferrimagnetic behavior below 60 K. However, a higher Ni:Mn ratio induces room-temperature superparamagnetic behavior in the spinel nanoparticles due to oxidation of Mn³⁺ ions to Mn⁴⁺ ions at the O_h sites. Beyond a certain limit ($x > 1.2$), Ni ions added to the reaction mixture cannot be incorporated into the spinel lattice; rather, they are reduced by ethylene glycol to produce Ni nanoparticles, which get oxidized to form NiO during air annealing. The magnetic behaviors of Ni_xMn_{3-x}O₄ nanoparticles depend strongly on the Ni fraction in them. Ni_xMn_{3-x}O₄ nanoparticles with high Ni content (Ni:Mn = 1:1) have lower magnetic anisotropy, which makes them superparamagnetic even at room temperature. The results presented in this work clearly demonstrate that the magnetic properties of Ni_xMn_{3-x}O₄ nanoparticles can be easily tuned by controlling their Ni contents through spin decompensation via substitution of Ni ions by Mn ions of either (2+ or 3+) valencies.

Author statement

J.L.O.Q. and J.A.R.R. conducted formal analysis of the samples and analyzed the acquired data. M. E.A.R. acquired and analyzed the magnetic data of the samples. A.R. and S.D. synthesized the nanostructures and performed XPS analysis. J.L.O.Q., J.A.R.R. and U.P. prepared the manuscript. J.L.O.Q. and U.P. were involved in conceptualization. U.P. & S.D. acquired the financial support for the project leading to this publication.

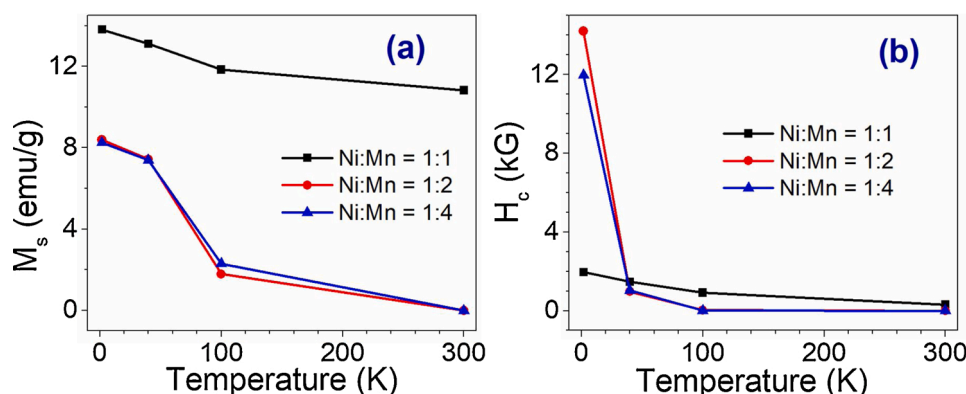


Fig. 9. Temperature variation of (a) saturation magnetization (M_s) and (b) coercive field (H_c) of the Ni_xMn_{3-x}O₄ nanoparticles containing different Ni:Mn ratios.

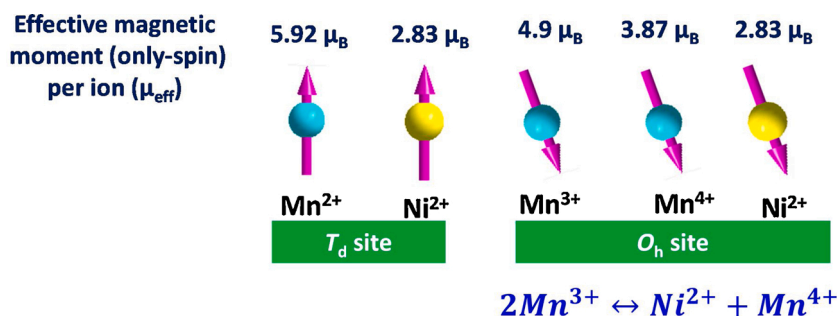


Fig. 10. Schematics of the magnetic moments and the noncollinear spin alignment of the cations present in $\text{Ni}_x\text{Mn}_{3-x}\text{O}_4$ at T_d and O_h sites. Substitution of Mn^{3+} ion at O_h site by Ni^{2+} ion and the consequent transformation to Mn^{4+} for maintaining lattice charge electroneutrality is presented at the bottom.

Table 4

Experimental and calculated M_s value for $\text{Ni}_x\text{Mn}_{3-x}\text{O}_4$ particles (nano- and micrometric) with different Ni:Mn ratios.

Material	Ni:Mn ratio	Av. size	M_s value ^a		Temp.(K)	Ref.
			Experimental	Calculated		
NiMn_2O_4	1:2	> 200 nm	14.47 emu/g (0.60 μ_B)	–	5	[19]
$\text{Ni}_{0.96}\text{Mn}_2\text{O}_4$	1:2.08	~ 1 μm	~35 emu/g (~1.44 μ_B)	0.87 μ_B	25	[15]
NiMn_2O_4 (with 6% NiO)	1:2	0.5–2 μm	30 emu/g (1.25 μ_B)	–	5	[18]
$\text{NiMn}_2\text{O}_{3.85}$	1:2	–	28 emu/g (1.15 μ_B)	–	5	[45]
NiMn_2O_4	1:2	–	36 emu/g (1.15 μ_B)	–	5	[48]
NiMn_2O_4	1:2	1–2 μm	37.5 emu/g (1.56 μ_B)	–	1.7	[46]
NiMn_2O_4	1:2	–	45 emu/g (1.87 μ_B)	–	5	[49]
$\text{Ni}_{0.75}\text{Mn}_{2.25}\text{O}_{4.5}$	1:3	–	18 emu/g (0.77 μ_B)	1.03 μ_B	5	[47]
$\text{Ni}_{0.5}\text{Mn}_{2.5}\text{O}_{4.5}$	1:5	–	31 emu/g (1.37 μ_B)	1.74 μ_B	5	[47]
$\text{Ni}_{1.5}\text{Mn}_{1.5}\text{O}_4$	1:1 ^b	~19 nm	13.1 emu/g (0.55 μ_B)	0.6 μ_B	1.8	this work
NiMn_2O_4	1:2	~15 nm	8.4 emu/g (0.35 μ_B)	1.2 μ_B	1.8	this work
$\text{Ni}_{0.6}\text{Mn}_{2.4}\text{O}_4$	1:4	~17 nm	8.2 emu/g (0.34 μ_B)	1.8 μ_B	1.8	this work

^a Values given in Bohr magnetons are per formula unit.

^b Ni:Mn molar ratio in the proposed cation distribution is 1:1.5.

Declaration of Competing Interest

The authors declare no conflicts of interest. All the authors have revised the final version of the manuscript and approved its submission.

Acknowledgements

This work was partially supported by CONACyT (Grants # INFR-2014-02-23053 & A1-S-26720), VIEP-BUAP (Grant # VIEP/EXC/2018), Mexico, and the Department of Science and Technology (DST), Government of India through the 'INSPIRE Faculty Award' (Grant #IFA13-PH-71). JLOQ thanks to CONACyT for the postdoctoral scholarship.

References

- J.L. Martín de Vidales, P. García-Chain, R.M. Rojas, E. Vila, O. García-Martínez, Preparation and characterization of spinel-type Mn-Ni-Co-O negative temperature coefficient ceramic thermistors, *J. Mater. Sci.* 33 (1998) 1491–1496.
- S. Fritsch, J. Sarrias, M. Brieu, J.J. Couderc, J.L. Baudour, E. Snoeck, A. Rousset, Correlation between the structure, the microstructure and the electrical properties of nickel manganite negative temperature coefficient (NTC) thermistors, *Solid State Ion.* 109 (1998) 229–237.
- G.D.C. Csete de Györgyfalva, A.N. Nolte, I.M. Reaney, Correlation between microstructure and conductance in NTC thermistors produced from oxide powders, *J. Eur. Ceram. Soc.* 19 (1999) 857–860.
- R. Schmidt, A. Basu, A.W. Brinkman, Z. Klusek, P.K. Datta, Electron-hopping modes in $\text{NiMn}_2\text{O}_{4+\delta}$ materials, *Appl. Phys. Lett.* 86 (2005), 073501.
- S. Guillemet-Fritsch, J. Salmi, J. Sarrias, A. Rousset, S. Schuurman, A. Lannoo, Mechanical properties of nickel manganites-based ceramics used as negative temperature coefficient thermistors (NTC), *Mater. Res. Bull.* 39 (2004) 1957–1965.
- A. Veres, J.G. Noudem, O. Perez, S. Fourrez, G. Bailleul, Manganese based spinel-like ceramics with NTC – type thermistor behaviour, *Solid State Ion.* 178 (2007) 423–428.
- A. Feteira, Negative temperature coefficient resistance (NTCR) ceramic thermistors: an industrial perspective, *J. Am. Ceram. Soc.* 92 (2009) 967–983.
- S. Periyasamy, P. Subramanian, E. Levi, D. Aurbach, A. Gedanken, A. Schechter, Exceptionally active and stable spinel manganese oxide electrocatalysts for urea oxidation reaction, *ACS Appl. Mater. Interfaces.* 8 (2016) 12176–12185.
- P.W. Menezes, A. Indra, O. Levy, K. Kailasam, V. Gutkin, J. Pfommer, M. Driess, Using nickel manganese oxide catalysts for efficient water oxidation, *Chemcomm* 51 (2015) 5005–5008.
- H. Wei, J. Wang, L. Yu, Y. Zhang, D. Hou, T. Li, Facile synthesis of NiMn_2O_4 nanosheet arrays grown on nickel foam as novel electrode materials for high-performance supercapacitors, *Ceram. Int.* 42 (2016) 14963–14969.
- L. Li, H. Hu, S. Ding, Facile synthesis of ultrathin and perpendicular NiMn_2O_4 nanosheets on reduced graphene oxide as advanced electrodes for supercapacitors, *Inorg. Chem. Front.* 5 (2018) 1714–1720.
- Y. Sun, J. Zhang, X. Sun, N. Huang, High-performance spinel NiMn_2O_4 microspheres self-assembled with nanosheets by microwave-assisted synthesis for supercapacitors, *CrystEngComm* 22 (2019) 1645–1652.
- W. Kang, Y. Tang, W. Li, X. Yang, H. Xue, Q. Yang, C.S. Lee, High interfacial storage capability of porous $\text{NiMn}_2\text{O}_4/\text{C}$ hierarchical tremella-like nanostructures as the lithium ion battery anode, *Nanoscale* 7 (2015) 225–231.
- S. Li, J. Xu, Z. Ma, S. Zhang, X. Wen, X. Yu, J. Yang, Z.-F. Ma, X. Yuan, NiMn_2O_4 as an efficient cathode catalyst for rechargeable lithium-air batteries, *Chemcomm* 53 (2017) 8164–8167.
- A. Díez, R. Schmidt, A.E. Sagua, M.A. Frechero, E. Matesanz, C. Leon, E. Morán, Structure and physical properties of nickel manganite NiMn_2O_4 obtained from nickel permanganate precursor, *J. Eur. Ceram. Soc.* 30 (2010) 2617–2624.
- M.H. Ouaguenouni, A. Benadda, A. Kiennemann, A. Barama, Preparation and catalytic activity of nickel-manganese oxide catalysts in the reaction of partial oxidation of methane, *Comptes Rendus - Chim.* 12 (2009) 740–747.
- G. Ashcroft, I. Terry, R. Gover, Study of the preparation conditions for NiMn_2O_4 grown from hydroxide precursors, *J. Eur. Ceram. Soc.* 26 (2006) 901–908.
- A.J.F. Cabral, J.P. Serna, B.R. Salles, M.A. Novak, A.L. Pinto, C.M.R. Remédios, Exchange bias effect in polycrystalline $\text{NiO}/\text{NiMn}_2\text{O}_4$ composite, *J. Alloys. Compd.* 630 (2015) 74–77.
- M. Tadic, S.M. Savic, Z. Jaglicic, K. Vojisavljevic, A. Radojkovic, S. Prsic, D. Nikolic, Magnetic properties of NiMn_2O_4 (nickel manganite): Multiple magnetic phase transitions and exchange bias effect, *J. Alloys. Compd.* 588 (2014) 465–469.
- D. Larcher, R. Patrice, Preparation of metallic powders and alloys in polyol media: a thermodynamic approach, *J. Solid State Chem.* 154 (2000) 405–411.
- M.M. Natile, A. Glisenti, New $\text{NiO}/\text{Co}_3\text{O}_4$ and $\text{Fe}_2\text{O}_3/\text{Co}_3\text{O}_4$ nanocomposite catalysts: synthesis and characterization, *Chem. Mater.* 15 (2003) 2502–2510.
- R.A. Ferreira, J.C.G. Tedesco, J.O. Birk, W. Kalfceff, F. Yokaiichiya, N. Rasmussen, O. Peña, P.F. Henry, G.G. Simeoni, H.N. Bordallo, P.N. Lisboa-filho,

- Ferrimagnetism and spin excitation in a Ni-Mn partially inverted spinel prepared using a modified polymeric precursor method, *Mater. Chem. Phys.* 146 (2014) 58–64.
- [23] S. Asbrink, A. Waikowskat, E. Taliks, Physical properties and X-ray diffraction of a NiMn₂O₄ single crystal below and above the ferrimagnetic transition at T_c = 145 K, *J. Phys. Chem. Solids* 58 (1997) 725–729.
- [24] G. Rogers, Burns, *Mineralogical Applications of Crystal Field Theory*, 2nd ed., Cambridge University Press, Cambridge, 1993.
- [25] R.D. Shannon, Revised effective ionic radii and systematic studies of interatomic distances in halides and chalcogenides, *Acta Crystallogr., Sect. A* 32 (1976) 751–767.
- [26] J.E. Huheey, E.A. Keiter, Richard L. Keiter, *Inorganic Chemistry: Principles of Structure and Reactivity*, 4th ed., HarperColling College Publishers, New York, 1993.
- [27] J.F. Moulder, W.F. Stickle, P.F. Sobol, B.D. Kenneth, *Handbook of X-ray Photoelectron Spectroscopy*, 1st ed., Perkin-Elmer Corporation, Eden Prairie, 1992.
- [28] T. Hashemi, A.W. Brinkman, X-ray photoelectron spectroscopy of nickel manganese oxide thermistors, *J. Mater. Res.* 7 (1992) 1278–1282.
- [29] J. Topfer, A. Feltz, D. Graf, B. Hackl, L. Raupach, P. Weissbrodt, Cation valencies and distribution in the spinels NiMn₂O₄ and M₂Ni_{2-x}O₄ (M=Li, Cu) studied by XPS, *Phys. Status Solidi* 134 (1992) 405–415.
- [30] W. Ren, Y. Zhang, N. Zhu, A. Feng, S. Shang, Synthesis of NiMn₂O₄ thin films via a simple solid-state reaction route, *Ceram. Int.* 46 (2020) 11675–11679.
- [31] R.N. Jadhav, V. Puri, Microwave absorption, conductivity and complex permittivity of fritless Ni_(1-x)Cu_xMn₂O₄ (0 ≤ x ≤ 1) ceramic thick film: effect of copper, *Prog. Electromagn. Res. C* 8 (2009) 149–160.
- [32] J. Preudhomme, P. Tarte, Infrared studies of spinels-III, the normal II-III spinels, *Spectrochim. Acta.* 27A (1971) 1817–1835.
- [33] S. Bernardini, F. Bellatreccia, A. Casanova Municchia, G. Della Ventura, A. Sodo, Raman spectra of natural manganese oxides, *J. Raman Spectrosc.* 50 (2019) 873–888.
- [34] C. Julien, M. Massot, S. Rangan, M. Lemal, D. Guyomard, Study of structural defects in γ-MnO₂ by Raman spectroscopy, *J. Raman Spectrosc.* 33 (2002) 223–228.
- [35] N. Mironova-Ulmane, A. Kuzmin, I. Steins, J. Grabis, I. Sildos, M. Pärs, Raman scattering in nanosized nickel oxide NiO, *J. Phys. Conf. Ser.* 93 (2007), 012039.
- [36] N. Mironova-Ulmane, A. Kuzmin, I. Steins, J. Grabis, I. Sildos, M. Pärs, Raman scattering in nanosized nickel oxide NiO, *J. Phys. Conf. Ser.* 93 (2007) 1–5.
- [37] L. Malavasi, P. Galinetto, M.C. Mozzati, C.B. Azzoni, G. Flor, Raman spectroscopy of AMn₂O₄ (A = Mn, Mg and Zn) spinels, *Phys. Chem. Chem. Phys.* 4 (2002) 3876–3880.
- [38] L.I. Granone, A.C. Ulpe, L. Robben, S. Klimke, M. Jahns, F. Renz, T.M. Gesing, T. Bredow, R. Dillert, D.W. Bahnemann, Effect of the degree of inversion on optical properties of spinel ZnFe₂O₄, *Phys. Chem. Chem. Phys.* 20 (2018) 28267–28278.
- [39] X. Jiang, Y. Wang, T. Herricks, Y. Xia, Ethylene glycol-mediated synthesis of metal oxide nanowires, *J. Mater. Chem.* 14 (2004) 695.
- [40] D. Sellmyer, R. Skomski, *Advanced Magnetic Nanostructures*, 1st ed., Springer, New York, 2006.
- [41] B.D. Cullity, C.D. Graham, *Introduction to Magnetic Materials*, 2nd ed., Wiley, Hoboken, New Jersey, 2009.
- [42] Menaka, N. Garg, S. Kumar, D. Kumar, K.V. Ramanujachary, S.E. Lofland, A. K. Ganguli, Nanostructured nickel manganese oxide: aligned nanostructures and their magnetic properties, *J. Mater. Chem.* 22 (2012) 18447–18453.
- [43] G.F. Goya, H.R. Rechenberg, J.Z. Jiang, Magnetic irreversibility and relaxation in CuFe₂O₄ nanoparticles, *J. Magn. Magn. Mater.* 218 (2000) 221–228.
- [44] M. Bououdina, K. Omri, M. El-Hilo, A. El Amiri, O.M. Lemine, A. Alyamani, E. K. Hlil, H. Lassri, L. El Mir, Structural and magnetic properties of Mn-doped ZnO nanocrystals, *Phys. E Low-Dim. Syst. Nanostruct.* 56 (2014) 107–112.
- [45] D. Alburquenque, L. Troncoso, J.C. Denardin, A. Butera, K.D. Padmasree, J. Ortiz, F. Herrera, J.F. Marco, J.L. Gautier, Structural and physicochemical properties of nickel manganite NiMn₂O_{4-δ} synthesized by sol-gel and ultra sound assisted methods, *J. Alloys. Compd.* 672 (2016) 307–316.
- [46] A.J. Freitas-Cabral, C.R. Remédios, X. Grates, V.A. Chitta, Effects of microstructure on the magnetic properties of polycrystalline NiMn₂O₄ spinel oxides, *J. Magn. Magn. Mater.* 469 (2019) 108–112.
- [47] D. Alburquenque, L. Troncoso, J.C. Denardin, J.F. Marco, J.L. Gautier, Cation distribution and magnetic properties of Ni_xMn_{3-x}O_{4.δ} (x = 0.5, 0.75) synthesized by an ultrasound method, *J. Phys. Chem. Solids* 134 (2019) 89–96.
- [48] H. Goto, J. Fukushima, H. Takizawa, Control of magnetic properties of NiMn₂O₄ by a microwave magnetic field under air, *Materials (Basel)* 9 (2016) 169.
- [49] A.J. Freitas-Cabral, R.C.M. Remédios, C.A. Ospina, A.M.G. Carvalho, S. L. Morelha, Structure of antiferromagnetic NiO/ferrimagnetic NiMn₂O₄ composite prepared by sorbitol-assisted sol-gel method, *J. Alloys. Compd.* 696 (2017) 304–309.
- [50] M.S. Bazarjani, M.M. Muller, H. Kleebe, Y. Juttke, I. Voigt, M.B. Yazdi, L. Alff, R. Riedel, A. Gurlö, High-temperature stability and saturation magnetization of superparamagnetic nickel nanoparticles in microporous polysilazane-derived ceramics and their gas permeation properties, *ACS Appl. Mater. Interfaces* 6 (2014) 12270–12278.
- [51] N. Rinaldi-Montes, P. Gorria, D. Martínez-Blanco, A.B. Fuertes, I. Puente-Orench, L. Olivi, J.A. Blanco, Size effects on the Néel temperature of antiferromagnetic NiO nanoparticles, *APL Adv.* 6 (2016), 056104.
- [52] G. Srinivasan, M.S. Seehra, Magnetic properties of Mn₃O₄ and a solution of the canted-spin problem, *Phys. Rev. B* 28 (1983) 1–7.
- [53] W.S. Seo, H.H. Jo, K. Lee, B. Kim, S.J. Oh, J.T. Park, Size-dependent magnetic properties of colloidal Mn₃O₄ and MnO nanoparticles, *Angew. Chemie Int. Ed.* 43 (2004) 1115–1117.
- [54] M.T. Hutchings, E.J. Samuelsen, Measurement of spin-wave dispersion in NiO by inelastic neutron scattering and its relation to magnetic properties, *Phys. Rev. B* 6 (1972) 3447–3461.
- [55] C.E. Housecroft, A.G. Sharpe, *Inorganic Chemistry*, Pearson Education Limited, Harlow, England, 2012.
- [56] P.N. Lisboa-Filho, M. Bahouta, P. Barahona, C. Moure, O. Peña, Oxygen stoichiometry effects in spinel-type NiMn₂O_{4-δ} samples, *J. Phys. Chem. Solids* 66 (2005) 1206–1212.
- [57] Y. Shen, T. Nakayama, M. Arai, O. Yanagisawa, M. Izumi, Magnetic phase transition and physical properties of spinel-type nickel manganese oxide, *J. Phys. Chem. Solids* 63 (2002) 947–950.
- [58] J.M.D. Coey, *Magnetism and Magnetic Materials*, 1st ed., Cambridge University Press, New York, 2009.
- [59] John Goodenough, *Magnetism and Chemical Bond*, 1st ed., Interscience Publishers, New York, 1963.
- [60] A. Feltz, J. Töpfer, Investigations on electronically conducting oxide systems XXVI. Preparation and properties of Ni₆MnO₈ and NiMnO_{3.8} (δ ≈ 0.02), *J. Alloys. Compd.* 196 (1993) 75–79.